# Journal of Materials Chemistry C

Accepted Manuscript


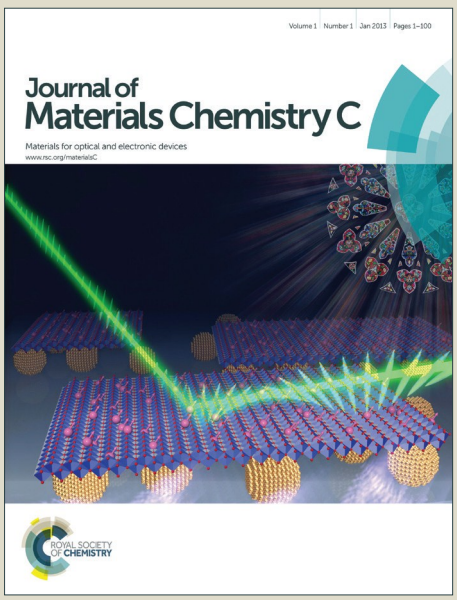





ROYAL SOCIETY OF CHEMISTRY

www.rsc.org/materialsC

Journal of Materials Chemistry C

ARTICLE

# High porosity scaffold composites of Graphene and Carbon Nanotubes as microwave absorbing materials.

Received 00th January 20xx,
Accepted 00th January 20xx

DOI: 10.1039/x0xx00000x

www.rsc.org/

M. González, J. Baselga, J. Pozuelo*

The design of microwave absorbing materials requieres low reflection and high absorption of radiation simultaneously. Low reflection can be achieved inducing porous faces which minimize the impedance mismatch. High absorption can be obtained increasing the conductivity of the material. We report the preparation of highly porous scaffolds formed by the combination of graphene and carbon nanotubes. The bimodal porous structure was controlled making use of the surface properties of graphene oxide that are able to stabilize hexane droplets in aqueous dispersions of graphene oxide and carbon nanotubes. After hydrothermal and two step freeze-drying processes , macro (220 microns) and mesoporous (10 microns) structures, due to the hexane droplets and the freeze drying respectively, were obtained. DC conductivities of 8.2, 14.7, 33.2, 60.7 S/m were obtained for graphene scaffolds containing 0, 10, 20 and 40% of carbon nanotubes respectively. An electromagnetic characterization was performed on scaffolds infiltrated with epoxy resin; using appropriate models, the electromagnetic properties of the conducting phase have been obtained. Scaffolds with a thickness of 9 mm, were able to absorb up to 80% of the incident radiation keeping reflection as low as 20%.

## Introduction

There is a current strong interest in the development of microwave absorbers and shielding materials due to the increasing environmental electromagnetic pollution.[1,2] There are three possible interactions of electromagnetic waves with matter. When the wave reaches the front-face of the material part of the incident power is reflected and the non-reflected power is transmitted through the sample; the transmitted portion can be absorbed or transmitted out from the slab. Partial reflection occurs when the incident electromagnetic wave propagating through a medium with impedance $Z_0$, reaches the surface of a material with different impedance $Z_M$. The reflected power depends on the impedance mismatch and falls to zero when $Z_M = Z_0$.[3] The absorbed power also depends on the impedance of the material, that is, both the reflection and absorption processes are favoured in materials with high conductivity. However, if the reflection losses are high, only a small portion of the radiation is able to penetrate into the material and therefore the material will not behave as an efficient absorber. Porous conductive materials decrease the impedance mismatch between the medium and the material, and are, therefore an alternative for the preparation of microwave absorbers.

In a previous report[4] we prepared porous CNT scaffolds from aqueous CNT dispersions using chitosan as organic binder. Power analysis revealed particularly low transmitted power (less than 10%) and high absorbed power (close to 70%). More interestingly, samples with the highest pore size and porosity presented the lowest and highest reflected and absorbed power respectively. The presence of a dielectric (chitosan) at the CNT interfaces limited both the conductivity and absorption behaviour at low frequencies (below 8 GHz). In this paper, we present novel porous structures in which chitosan is substituted by graphene which acts as the CNT binder and as a surfactant controlling the pore size and stabilizing the scaffold's structure.

Graphene oxide (GO) is formed by oxidized graphene amphiphilic fragments which present a random distribution of aliphatic and aromatic regions.[5] GO possess hydrophilicity due to the presence of oxidized aliphatic regions containing tetrahedral $sp^3$ carbon atoms, whereas hydrophobicity is due to the presence of aromatic regions with benzene rings containing planar sp2 carbon atoms.[6] It contains numerous functional groups mainly epoxy and hydroxyl groups on the plane, whereas carboxyl, carbonyl, ester, ether, diol, ketone, phenol, quinine and lactones groups are present at the edge surfaces of the GO sheets.[7] The oxidized functionalities present on the basal and edge planes render it for the high dispersion in aqueous solutions and pave a way for the chemical functionalization,[5] such as amidation at the carboxylic groups[8] or nucleophilic substitution via epoxy groups.[9] On the other hand, the aromatic regions having $sp^2$ networks provide active

*Departamento de Ciencia e Ingeniería de Materiales e Ingeniería Química (IAAB), Universidad Carlos III de Madrid, 28911 Leganés, Madrid, Spain.*
**Javier Pozuelo. E-mail: jpozue@ing.uc3m.es; Fax:+34 91 6249430.*

Electronic Supplementary Information (ESI) available: Image of hexane droplets dispersed in GO solution; FTIR spectra of GO and GR XRD patterns and Raman spectra of the graphene and carbon nanotubes; Scheme of Hydrogenated Bisphenol A diglycidyl ether (HDGEBA) and m-Xylylenediamine; Glass transition temperatures of GR:CNT:HDGEBA:mXD composites; Transmission coefficient GR:CNT:HDGEBA:mXD composites. See DOI: 10.1039/x0xx00000x

sites to interact with other aromatic molecules through π-π supramolecular interactions.[10]

Self-assembly and reduction of GO into interconnected graphene networks is simultaneously achieved by heat treating aqueous GO suspensions for a certain amount of time inside a teflon-lined autoclave.[11,12] During the hydrothermal process, the oxygen contained in the functional groups of GO is gradually eliminated, and the conjugated structures are restored. The growing hydrophobicity and π-π interactions between reduced graphene cause a random self-assembly of the flexible sheets in 3D-hydrogels with pore size distribution from sub-micrometres to a few micrometres.[13,14]

In addition, it has been proved that GO is a good CNT dispersant forming stable dispersions of CNT; the resulting dispersion is a novel hybrid named as graphene oxide-CNT (GO-CNT).[15] Some studies have also proved that GO-CNT and graphene-CNT hybrid nanomaterials exhibit higher electrical conductivities, large specific area and catalytic properties compared with either pristine CNTs or GO/graphene.[16,17] If an amount of oxidized CNT is added to GO dispersions, monoliths obtained after the hydrothermal process are formed by both compounds. The strong π-π stacking interaction operating between graphene planar fragments and between graphene and CNT provides an exceptional stability to the 3D network of the resulting hybrid material.[18]

To control the pore size and to obtain hierarchical pore morphology we have modified an already reported hydrothermal method[19] which involves the preparation of stable aqueous emulsions of graphene oxide containing hexane droplets. A subsequent careful cold evaporation of hexane followed by lyophilisation of the aqueous phase allows achieving more consistent scaffold structures and displaces and compresses the CNT-rGO towards the walls of the ice crystal structure increasing the CNT connectivity and, consequently, the conductivity of material.

## Experimental.

### Materials.

Graphite powder (with a purity >99.999%) was purchased from Alfa Aesar. Multi-walled carbon nanotubes Graphistrength® C100 (with a purity >90%) were purchased from Arkema Inc. Hexane (Panreac) was used as organic phase. The hydrogenated derivative of diglycidyl ether of bisphenol-A (HDGEBA) epoxy resin was supplied by CVC Specialty Chemicals (USA); its epoxy equivalent mass was 210 $g \cdot mol^{-1}$ determined by acid titration. m-Xylylenediamine (Sigma-Aldrich) was used as curing agent. $H_2O_2$ 30% w/v (Panreac), $KMnO_4$ (Panreac), $NaNO_3$ (Sigma-Aldrich) and $H_2SO_4$ 98% v/v (Panreac) were employed for graphite and CNT oxidation and used without any further purification.


Figure 1. Schematic illustration of the synthetic process of GR:CNT hybrid scaffold with high porosity.

### Hybrid composites preparation.

GO was prepared by a modified Hummer´s method.[20] In a typical experiment a 500 mL flask equipped with a thermometer and cooled in an ice-water bath was fed with 4 g of graphite and 2 g of $NaNO_3$; 180 mL of concentrated $H_2SO_4$ was added to the flask and stirred for 2 hours. Then, 11 g of $KMnO_4$ were added slowly to the mixture. The rate of addition was carefully controlled to keep the reaction temperature below 20 ˚C. After adding the oxidant, the ice-water bath was removed and stirring was continued for 2 hours at room temperature. The oxidation process was stopped adding very slowly 180 mL of $H_2O$. As the reaction temperature rapidly increased to 80˚C, 30 mL of 30% $H_2O_2$ were added to the mixture. For purification, the mixture was washed rinsing with distilled water and centrifuging at 4500 rpm for 30 min several times until the pH of the solution was 6-7. After freeze-drying, GO was obtained as a solid.

To remove the extreme CNT hydrophobicity while keeping their aspect ratio, oxidation with $H_2O_2$/UV was performed.[21] In a typical experiment, 100 mL of $H_2O_2$ (30% wt) was added to 1 g of CNT keeping the mixture in an ultrasonic bath for three minutes; then the mixture was exposed to UV light (Philips Lighting 250HPLN 250W) for 15 minutes stirring with a magnetic stirrer. The dispersion was filtered and washed three times with distilled water and finally dried under vacuum. Scaffolds were prepared by a modified hydrothermal reduction method reported by Li et al.[19]

Figure 1 shows a schematic illustration of the synthetic process. Aqueous dispersions of GO:CNT were prepared with a total concentration of carbonaceous nanoparticles of 5 mg/mL, varying the proportion of CNT from 0 to 40%. In a typical experiment, 8 mL of an aqueous dispersion was mixed with 4 mL hexane and shook vigorously to form a homogeneous emulsion. The emulsion was sealed in a 20 mL Teflon autoclave and maintained at 180 °C for 10 h; afterwards the autoclave was naturally cooled to room temperature and the hexane containing gel was removed. Attempts to remove hexane solvent via the hot water treatment[19] were not successful because of the collapse of the macropores. Alternatively, we found that a previous hexane cold evaporation under vacuum with the scaffold, frozen at -10 °C was a successful approach. After hexane was completely

removed freeze-drying of the frozen hexane-free scaffold was performed to avoid serious volume shrinkage during the process of water removal and to preserve the shape and porous 3D structure.[22]

**Techniques.**

GO, GR, CNT and GR:CNT were characterized by Wide-Angle X-Ray Diffraction (XRD, Panalytical X´pert Pro X-ray diffractometer with Cu Kα radiation, λ = 0.15406 nm). SEM images were obtained with a Philips XL 30 scanning electron microscope. X-ray photoelectron spectroscopy (XPS) was carried out using ESCAPROBE P with a monochromatized Mg X-ray source (1253.6 eV photons) and a hemispherical analyser Omicron EA125 to analyse the chemical composition of the composites. Raman spectroscopy was carried out with an inVia confocal Raman microscope (Renishaw) using the 514.5 nm laser excitation. For each sample, various spectra were recorded in different places in order to verify the homogeneity of the sample. Thermogravimetric analysis (TGA) was carried out using a simultaneous thermal analyser Perkin Elmer 6000STA under air atmosphere from room temperature to 1000˚C at 10˚Cmin$^{-1}$. Differential Scanning Calorimetry (Mettler Toledo DSC 822e) was used to measure the Tg of the epoxy resin. Electrical properties of the composites were evaluated using a HP 34401A source meter with 100 μΩ resolution. Measurements were performed in 4-wire DC configuration to obviate the electrical resistance of the wires. The temperature of the samples during the measurement was 25˚C.

The global electromagnetic shielding efficiency, $SE_T$, can be quantified as the sum of the contributions of reflection and absorption mechanisms. For this purposes, the scattering parameters $S_{11}$ and $S_{21}$ were determined using a vector network analyzer (Agilent, ENA, E5071) with a 7 mm coaxial transmission line adapter in the range of 1 to 18 GHz. An ENA instrument measures both the transmitted and reflected power coefficients ($T=|S_{21}|^2=|S_{12}|^2$ and $R=|S_{11}|^2=|S_{22}|^2$), therefore the absorbed power coefficient by the material (A) is:

$$\boldsymbol{A = 1 - (R + T)} \quad (2)$$

The ratios between the scattering parameters and the transmission, reflection and absorption EMI shielding effectiveness are given by the following equations.

$$\boldsymbol{SE_T = -10log(T) = -10log(|S_{21}|^2)} \quad (2)$$

$$\boldsymbol{SE_R = -10log(1 - R) = -10log(1 - |S_{11}|^2)} \quad (3)$$

$$\boldsymbol{SE_A = -10log\left(\frac{T}{1-R}\right) = -10log\left(\frac{|S_{21}|^2}{1-|S_{11}|^2}\right)} \quad (4)$$

The scattering parameters were also used to calculate the complex magnetic permeability and dielectric permittivity of the hybrid composites. The measurements were performed according to the transmission/reflection method.[23] For electromagnetic characterization, the scaffolds were vacuum infiltrated with an epoxy resin, as described previously,[24] cured and machined to the final required geometry for the coaxial line: rectangular toroids of nominal internal and external diameters close to 3.04 and 7 mm respectively. Using the built-in software, a geometry correction was applied for small deviations from nominal geometry.[23]

## Results and discussion.

**Scaffolds Characterization.**

Interfacial tension in the water/n-hexane system is rather high (~51 mN·m$^{-1}$) and their mixtures quickly demulsify when stirring is stopped.[25] However, in the presence of GO, the suspensions remain stable for long periods of time (>6 months). As already mentioned, the partially disrupted 2D $sp^2$ lattice characteristic of GO sheets contains oxidized functionalities mainly at their edges[20] which confer amphiphilic properties to the sheets. GO, therefore adsorbs on the surface of hexane droplets and other nonpolar solvents acting as an emulsion stabilizer and preventing their breakdown and coalescence from water suspensions.[7,26] This effect also remains when GO is partially substituted by CNT with droplet mean side of 212 microns (see supplementary information).

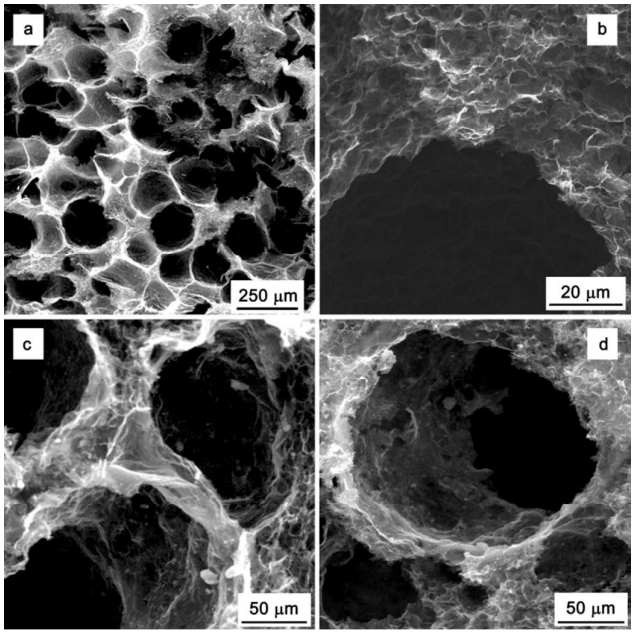


Figure 2. SEM images of hierarchical distribution of pore sizes: macropores formed around the n-hexane soft template drops a,b). GR, c) GR:CNT10%, d)GR:CNT40%

During the hydrothermal process the graphene oxide sheets are reduced and assembled around the hexane droplets which act as soft templates for macroporous structures.[19] The hybrid aerogels exhibit a three-dimensional network structure

composed of hierarchical distribution of pores. SEM images shown in of Figure 2 reveal big pores with a diameter of 220 ± 40 microns irrespective of the CNT content (see supplementary information). These pores are embedded in the aerogel matrix and their walls are composed of randomly oriented CNT, wrinkled graphene sheets and a lot of micropores with a mean diameter of 5 ± 1.5 microns enclosed by CNT´s and graphene sheets. The macropores are formed by the collapse of the carbonaceous constituents around the n-hexane soft template droplets and the micropores, as already reported, are attributed to water exclusion due to the collapse of graphene sheets during the hydrothermal process.[13] It is worth noting that the macropore size do not experience any substantial change during the hydrothermal process.

XRD patterns of the graphene and carbon nanotubes before and after of the hydrothermal treatment are shown in Figure 2SI (supplementary information). The typical diffraction peak for GO before dispersion appears at around 12˚ while after hydrothermal treatment shifts to 23.78˚, indicative of graphitic structures. Nevertheless, the d-spacing in the aerogel (0.382 nm) is still slightly larger than in the well-ordered graphite (0.335 nm).[27] These results suggest the partial reduction of GO in the hydrothermal reduction and the existence of π-π stacking between graphene sheets after hydrothermal treatment.[26]

Oxidized carbon nanotubes (CNTox) XRD pattern shows two intense peaks at scattering angles of 26.1˚ and 44.25˚ which correspond to (0 0 2) and (1 0 1) planes of hexagonal graphite respectively. Some other low intensity peaks corresponding to remaining catalyst iron oxides can be observed also. Hydrothermal treatment does not affect the structure and composition of the CNT showing a similar interlayer spacing of 0.413 nm.

The reduction process of GO and CNTox were evaluated by X-ray photoelectron spectroscopy (XPS). Figure 3 and Table 1 reveal that: a) the hydrothermal treatment of graphene involves a significant decrease of C-O signal, confirming that most of the epoxide and hydroxyl groups were successfully removed; b) unsaturated and aliphatic carbon almost doubles its amount; c) the amount of oxygen is reduced to about half its initial value. These results confirm that the supercritical water produced in the hydrothermal condition plays the role of reducing agent and offers an effective reduction approach for graphene oxide.[26] By contrast; oxidized carbon nanotubes show no significant changes after HT.

GO and GR were characterized by FTIR (supplementary information). FTIR shows that absorption peaks at 3430 $cm^{-1}$ (the O–H stretching mode), 1726 $cm^{-1}$ (the C=O stretching mode), 1629 $cm^{-1}$ (the C=C stretching mode), 1365 $cm^{-1}$ (the C–OH stretching mode) and 1054 $cm^{-1}$ (the C–O stretching mode).[28] After the hydrothermal treatment, the intensities of these absorption peaks decrease compared with those in the GO, indicating the restoration of a graphitic structure in graphene consistently with XRD and XPS results.

Table 1: Compositional analysis by XPS.

| | | GO | GR | CNTox | CNT |
|---|---|---|---|---|---|
| Carbon atoms, % | C=C | 34,9 | 59,9 | 72,1 | 68,6 |
| | C-C | 8,1 | 15,0 | 6,7 | 6,2 |
| | C-O | 47,8 | 9,1 | 7,2 | 12,0 |
| | C=O | 6,5 | 6,5 | 5,1 | 4,8 |
| | COO | 2,3 | 4,9 | 3,5 | 3,4 |
| | π→π* | 0,4 | 4,7 | 5,4 | 5,0 |
| | C(1) | 76,2 | 88,9 | 98.2 | 98,0 |
| Oxygen atoms, % | C=O | 6,8 | 47,2 | 62,7 | 79,3 |
| | C-O | 89,4 | 44,5 | 33,2 | 17,5 |
| | COO | 3,8 | 8,3 | 4,2 | 3,2 |
| | O(1) | 23,8 | 11,1 | 1,8 | 2,0 |

(1) Global ratio of C and O atoms.

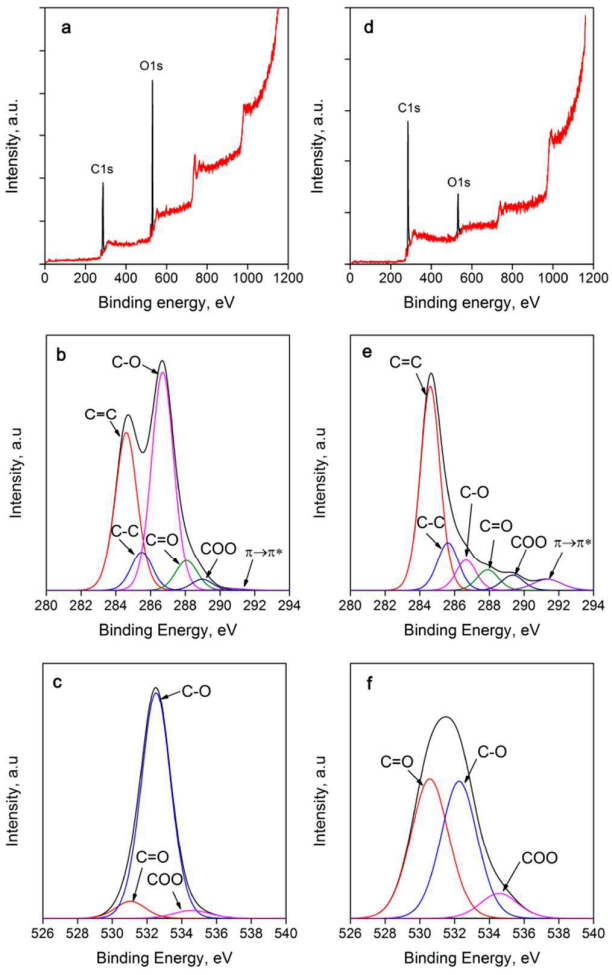


Figure 3. XPS spectra of (a) GO and (d) GR. C1s peak of GO (b) and GR (e). O1s peak of GO (c) and GR (f).

Raman spectra (supplementary information) show the two characteristic D and G bands located at about 1350 and 1590 $cm^{-1}$ respectively. G peak occurs due to bond stretching of $sp^2$ C-C bonds whereas the D peak is due to breathing of $sp^3$ C-C bonds in six-atom rings and requires defects for its activation. Similar $I_D/I_G$ ratios were obtained for CNTox and CNT (~1.20) and for GO and GR (1.0 -1.1).

**Electromagnetic characterization.**

The scaffolds were infiltrated with HDGEBA/m-Xylylenediamine (see supplementary information) for electromagnetic characterization. Cured samples were machined to the final required geometry for the coaxial line: rectangular toroids of internal diameter of 3.04-3.05 mm and external diameter of 6.95-7.00 mm. For evaluate the epoxy curing the glass transition temperatures were evaluated by DSC (supplementary information). No differences of glass transition temperatures were observed between epoxy resin (77.6˚C) and scaffold composites; therefore the scaffold does not affect the curing of the epoxy resin.

Although it is not precisely known how GR sheets are bonded during the hydrothermal treatment,[19] it is accepted that the sheets are located around the template droplets in a 2D fashion and packed in a thicker section as water is expelled. At the same time, although graphene becomes reduced, as already shown, the perfect hexagonal "graphene" framework cannot be completely recovered due to the existence of residual groups, defects and edges; therefore, the conductivity of GR should be lower than that of graphite.[29] Direct current conductivity, $\sigma_{DC}$, measurement of GR scaffold (0 % CNT) yields a value of: 8.2 S/m. Assuming a value of 1.8 $g/cm^3$ for the graphene density, the GR volume fraction in the scaffold is $\sim 10^{-2}$; assuming again an effective medium model for the conductivity of the scaffold, the true conductivity of the GR walls can be calculated as ~800 S/m. This value is between one and two orders of magnitude lower than reported conductivity data for graphite powders,[30] confirming thus that the graphene $sp^2$ framework has not been completely recovered.

DC conductivity data for scaffolds containing CNT are 14.7, 33.2 and 60.7 S/m for 10, 20 and 40 % CNT respectively. These results are higher than for the only-graphene scaffold and indicate that conductivity of composites increases with the CNT concentration probably due to the formation of more conductive CNT network paths and π-π interactions throughout the pore walls.

Permittivity will have the contribution of both, epoxy and GR-CNT, and hence, its value will be lower than that of a material exhibiting analogous conductivity values but being compact or non-porous.[31] These composites might exhibit low permittivities more similar to the epoxy resin than to a conductive material and will strongly depend on volume fraction of conductor phase.[32] It has been corroborated that the effective permittivity of aerogels, with almost all phase combinations, geometries and distributions, which are the less restrictive and depend on the volume fraction and the complex permittivity of each phase in the composite. The permittivity of composites with high epoxy fraction should be smaller than that due to the conductive filler.[33]

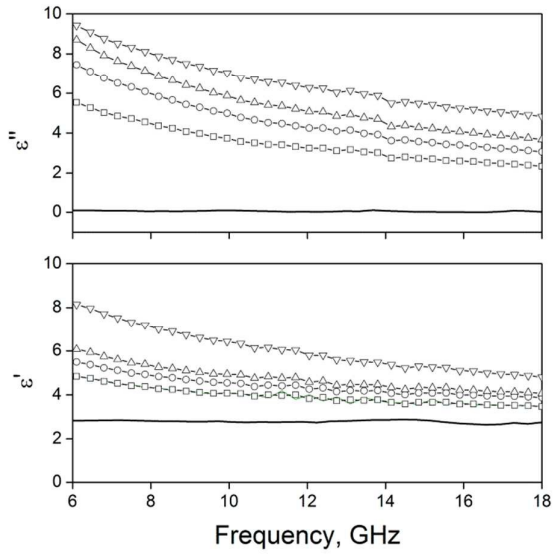


Figure 4. Dielectric permittivity of epoxy (line), and effective dielectric permittivity of GR (□), GR:CNT10% (○), GR:CNT20% (Δ), GR:CNT40% (∇).

Effective permittivity values are presented in Figure 4, along with the measured permittivity of pure epoxy, in which the real part (ε') represents the charge storage and the imaginary part (ε") is a measure of dielectric dissipation or losses. Both the real and imaginary parts decrease smoothly with frequency, a fact that is attributed to the Maxwell–Wagner polarization effect. This may arise from the reduction of the electric field induced in the porous composites in response to the reversing external electric field caused by the delay in the molecular polarization at higher frequency.[29] As it can be seen, the real (ε') and imaginary (ε'') permittivities grow as the concentration of CNT increases. These results are reasonable and can be attributed to the fact that the increasing content of CNT increases the dipolar polarization and electrical conductivity.[35] In the case of ε' this is a direct consequence of a higher number of interfaces prompt to polarization (Maxwell-Wagner-Sillars effect) associated to the migration and accumulation of charges at the conductive filler/polymer interfaces.[34] For ε", it is due to the reduction of the average distance between adjacent CNTs which, in turn, implies higher dielectric and ohmic losses.

However, the measured permittivity data are effective values of a mixture of two very different phases. To extract relevant information of the conducting phase, which cannot be measured due to its porous nature, it is possible to make use of the effective medium theory and the Maxwell-Garnett equation which relates the properties of the ensemble with the properties of each phase. This model is based on the

assumption that the structure of porous materials can be reasonably described as coated spheres and has been used to calculate effective permittivity of similar systems, i.e. silicon carbide foams[36,37] For an isotropic composite material consisting of two components (host and guest), the effective permittivity derived of model Maxwell-Garnett model can be expressed as:

$$\boldsymbol{\varepsilon_{eff}} = \boldsymbol{\varepsilon_1}\frac{(\varepsilon_2+2\varepsilon_1)+2\varphi_2(\varepsilon_2-\varepsilon_1)}{(\varepsilon_2+2\varepsilon_1)-\varphi_2(\varepsilon_2-\varepsilon_1)} \quad (5)$$

where $\varepsilon_1$ and $\varepsilon_2$ are electric permittivities of host (conductor phase) and guest (epoxy phase) and $\phi_2$ is the volume fraction of the epoxy.

From the results of effective permittivity of epoxy composites, real and complex permittivity of the conductive graphene and carbon nanotubes walls have been estimated. Figure 5 shows the calculated permittivity behaviour of this phase with frequency. It is possible to observe how the real part of the permittivity increases with the amount of carbon nanotubes mainly due to the increased interface extent between conductive fillers; additionally, values of the order of magnitude of graphite are obtained for the sample without nanotubes (GR).[38] This last result reflects the packing of GR platelets since the permittivity of a single graphene sheet is considerably lower, about 1.8 – 3.[39]

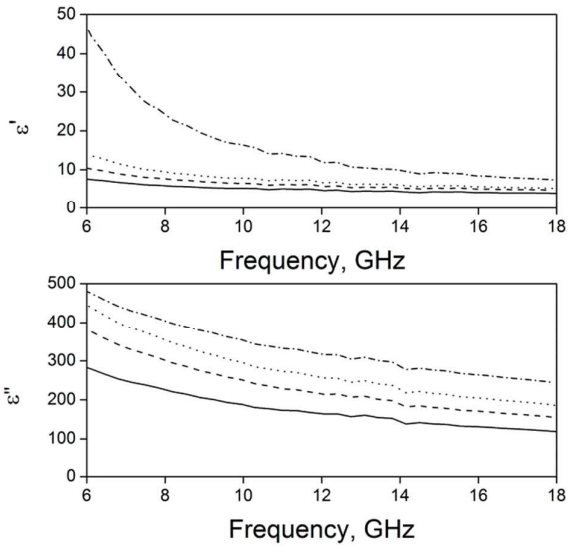


Figure 5. Dielectric complex permittivity of the conductive walls: GR (solid), GR:CNT10% (dash), GR:CNT20% (dot), GR:CNT40% (dash-dot).

However, the most remarkable result is the high value of ε'' for all the studied systems. The complex part of the permittivity is an order of magnitude greater than the real part. This suggests that the mechanism by which electromagnetic radiation is deactivated is essentially resistive. We can visualize this mechanism as set of reflections of incident radiation on the walls of the pores where it becomes partially deactivated through the generation of electrical current in each impact.

Three mechanisms for electromagnetic shielding are commonly accepted: reflection, absorption and multiple reflections.[3] Multiple reflections are produced by the coupling of the reflected radiation on the first incidence plane and reflection in the final plane of the material. This radiation coupling originates constructive and destructive wave interferences that are frequency dependent. According to SchelKunoff's theory multiple reflections can be neglected when the thickness of the slab is greater than the skin depth (δ),[40,41] which is the depth at which the incident field decreases at 1/e of its initial value. We estimate that in samples with a slab thickness of about three times the skin depth, multiple reflections may become negligible (see supplementary information), therefore, for our samples ((9 mm thickness) this mechanism may become negligible for frequencies higher to 6 GHz.

Figure 6 shows the reflected and absorbed power ($P_R$ and $P_A$) of the GR-CNT composites measured in the 6-18 GHz frequency range. In all cases the transmitted power was particularly low, not exceeding in any case 5% of incident power (Figure 6SI of supplementary information). Furthermore, the absorbed power was considerably greater than the power reflected by the material. These results indicate that all the measured systems can be considered as electromagnetic radiation absorbing materials. In our previous work[4], we demonstrated that the larger the pore size, the greater the absorption power. This is due to an increase in the ratio between the pore size and the size of the conductive wall that should cause a lower impedance mismatch between air and sample surface decreasing thus the reflected power.[42] The absorbed power is dependent on the power reflected; if the reflected power is very high the amount of radiation penetrating into the material is very small, and therefore the absorption will also be small. The reflected power depends mainly on the impedance mismatch between the medium and the plane of incidence of the material. Thus, small changes in porosity within the plane of incidence also cause considerable changes in the reflected power and therefore also in the absorbed power. Samples containing higher CNT are more reflective as a consequence of a higher electrical conductivity[43-45]. Therefore, the sample that only contains graphene presents the highest $P_A$ which decreases as the CNT content is increased due to the higher amount of reflected power.

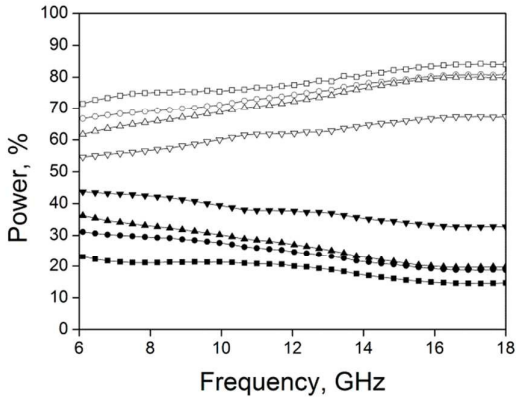


Figure 6. Reflection coefficient of GR0% (■), GR:CNT10% (●), GR:CNT20% (▲), GR:CNT40% (▼) and absorption coefficient of GR0% (□), GR:CNT10% (○), GR:CNT20% (Δ), GR:CNT40% (▽). Specimens with thickness of 9 mm.

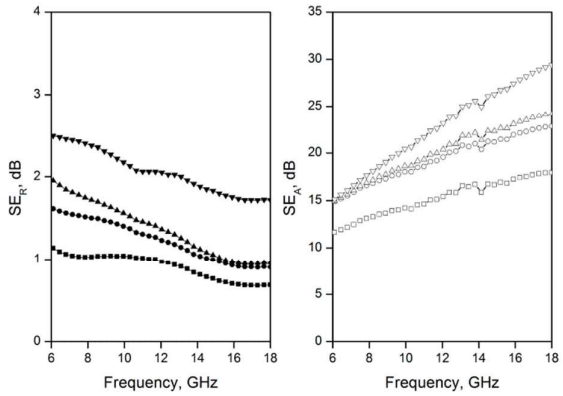


Figure 7. Reflection (left) and absorption (right) shielding efficiency of GR0% (■), GR:CNT10% (●), GR:CNT20% (▲), GR:CNT40% (▼).

The electromagnetic shielding mechanism was investigated through a shielding efficiency (SE) analysis (equations 2, 3 and 4). Figure 7 shows the SE due to reflection and absorption for the hybrid composites. $SE_R$ has negligible values in all the frequency range. $SE_A$ in contrast, increases with frequency for all samples, suggesting that absorption is the main electromagnetic dissipation mechanism.

Once the incident electromagnetic wave enters into the material, enhanced electrical conduction involves a better dissipation of energy across sample. When comparing the effect of the CNT concentration, it is observed that $SE_A$ (and $SE_T$, see supplementary information) increase with CNT content. Although this observation is consistent with previous reports about the electromagnetic shielding of CNT,[40] it may appear to be contradictory with the previous power analysis. However, it should be remarked that although high amounts of CNT could absorb more radiation because of its high conductivity, radiation can't penetrate due to reflection.

According to Al-Saleh et al.,[40] electromagnetic efficiency due to absorption is proportional to material thickness. Figure 8 shows a comparative study of $SE_A$ of graphene scaffold composites for three different thickness values (left) and the specific $SE_A$ in dB/cm (right) as a representative set. Other compositions give similar results. The three thicknesses appear to merge into a single curve although slight differences attributed to measurement errors and to slight differences in surface reflectivity can be observed. These results allow us to estimate the necessary thickness of a coating made by these methods to achieve optimal electromagnetic shielding for a specific application.

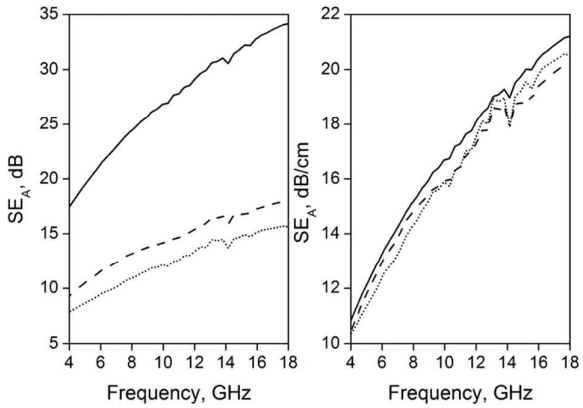


Figure 8. Absorbed shielding efficiency (left) of GR scaffold with composites thickness of: 16mm (line), 9 mm (dash), 6 mm (dots). Specific $SE_A$ in dB/cm (right) as a representative set.

## Conclusions.

GR/CNT hybrid composites with controlled porosity via a modified hydrothermal method (HT) have been successfully prepared as electromagnetic shielding materials in the GHz range. We have taken advantage of the surface activity of GO platelets to stabilize large hexane droplets in a water suspension during the high temperature hydrothermal reduction. In this way we have been able to obtain a bimodal porous structure as revealed by SEM analysis: a microporous structure (10 microns) due to HT and a macroporous structure (250 microns) due to the hexane droplets.

Characterization by XRD, Raman, XPS and FTIR has shown a reduction process in GO after HT without affecting the reduction state of CNT. Fitting effective permittivity data to Maxwell-Garnet model has allowed extracting relevant dielectric information on the conductive phase: as CNT content increases the dipolar polarization in the conductive phase also increase by Maxwell–Wagner–Sillars effect, and losses appear to level off for loadings higher than 20%. In all cases the

transmitted power with thickness of 9 mm was particularly low, not exceeding in any case 5% of incident power. In all cases, the absorbed power was significantly greater (close to 80% of incident power) than the power reflected (close to 20% of incident power). These results as well as shielding efficiency analysis allow us to affirm that all the studied systems can be considered as electromagnetic radiation absorbing materials.

## Acknowledgements

This work was supported by grant NANONARQ (MAT2014-57557-R) from the Spanish Ministerio de Economía y Competitividad.

## References

1 S. Biswas, G.P. Kar, S. Bose, *Nanoscale,* 2015, **7**, 11334-11351.
2 K. Singh, A. Ohlan, V.H. Pham, R. Balasubramanian, S. Varshney, J. Jang, S. H. Hur, W.M. Choi, M. Kumar, S.K. Dhawan, B.S Kong, J.S. Chung, *Nanoscale*, 2013, **5**, 2411-2420.
3 D. Chung, *Carbon*, 2001, **39**, 279-285.
4 M. González, M. Crespo, J. Baselga, J. Pozuelo, *Nanoscale*, 2016, **8**,10724-10730.
5 D.R. Dreyer, S. Park, C.W. Bielawski, R.S. Ruoff, *Chem. Soc. Rev*., 2010, **39**, 228-240.
6 L. Qiu, X. Yang, X. Gou, W. Yang, Z.F. Ma, *Chem. Eur. J.*, 2010, **16**, 10653-10658.
7 F. Kim, L.J. Cote, J. Huang, *Adv. Mater*., 2010, **22**, 1954-1958.
8 Z. Liu, J.T. Robinson, X. Sun, H. Dai, *J. Am. Chem. Soc*., 2008, **130**, 10876-10877.
9 H. Yang, F. Li, C. Shan, D. Han, Q. Zhang, L. Niu, A. Ivaska, *J. Mater. Chem*., 2009, **19**, 4632-4638.
10 Y. Xu, H. Bai, G. Lu, C. Li, G. Shi, *J. Am. Chem. Soc*., 2008, **130**, 5856-5857.
11 L. Zhang, F. Zhang, X. Yang, G. Long, Y. Wu, T. Zhang, K. Leng, Y. Huang, Y. Ma, A. Yu, Y. Chen, *Sci. Rep*., 2013, **3**, 1408.
12 Y. Xu, K. Sheng, C. Li, G. Shi, ACS Nano 2010, **4**, 4324-4330.
13 H. Gao, H. Duan, *Biosens. Bioelectron*., 2015, **65**, 404-419.
14 N. Cao, Y. Zhang, *J. Nanomaterials*, 2015, ID:168125.
15 V. Mani, B. Devadas, S.M. Chen, *Biosens. Bioelectron*., 2013, **41**, 309-315.
16 S.H. Lee, D.H. Lee, W.J. Lee, S.O. Kim, *Adv. Funct. Mater*., 2011, **21**, 1338-1354.
17 Y. Zhu, L. Li, C. Zhang, G. Casillas, Z. Sun, Z. Yan, G. Ruan, Z. Peng, A.R.O. Raji, C. Kittrell, R.H. Hauge, J.M. Tour, *Nat. Commun*., 2012, **3**, 1225.
18 V. Mani, S.M. Chen, B.S. Lou, *Int. J. Electrochem. Sci*., 2013, **8**, 11641-11660.
19 Y. Li, J. Chen, L. Huang, C. Li, J.D. Hong, G. Shi, *Adv. Mater*., 2014, 26, 4789-4793.
20 L. Shahriary, A. Athawale, *Int. J. Renew. Energy Environ. Eng*., 2014, **02**, 58-63.
21 O. Martín, H.R. Gutierrez, A. Maroto-Valiente, M. Terrones, T. Blanco, J. Baselga, *Mater. Chem. Phys*., 2013, 140, 499-507.
22 R. Lv, E. Cruz-Silva, M. Terrones, *ACS Nano*. 2014, **8**, 4061-4069.
23 Agilent 85071E Materials Measurement Software.
24 M. Crespo, N. Méndez, M. González, J. Baselga, J. Pozuelo, *Carbon*, 2014, **74**, 63-72.
25 G. M. Kontogeorgis, S. Kiil. Introduction to Apllied Colloid and Surface Chemistry. Chap. 3: Surface and Interfacial Tensions-Principles and Estimation Methods. Wiley (2016) Page 71.
26 P. Guo, H. Song, X. Chen, *J Mater Chem.* 2010, **20**, 4867.
27 H. Hu, Z. Zhao, W. Wan, Y. Gogotsi, J. Qiu, *Adv. Mater*., 2013, **25**, 2219-2223.
28 J.W. Jang, S. Cho, G.H. Moon, K. Ihm, J.Y. Kim, D.H. Youn, S. Lee, Y. Lee, W. Choi, K.H. Lee, J.S. Lee, *Chem - A Eur J*., 2012, **18**, 2762-2767.
29 C. Wang, X. Han, P. Xu, X. Zhang, Y. Du, S. Hu, J. Wang, X. Wang, *Appl. Phys. Lett*. 2011, **98**, 2011-2014.
30 N. Deprez, D.S. McLachlan, *J. Phys. D: Appl. Phys.,* 1988, **21**, 101-107.
31 Q. Liu, D. Zhang, T. Fan, *Appl. Phys. Lett.,* 2008, **93**, 013110.
32 L.W. Hrubesh, L.E. Keene, V.R. Latorre, *J. Mater. Res*., 1993, **8**, 1736.
33 F. Moglie, D. Micheli, S. Laurenzi, M. Marchetti, V. Mariani Primiani, *Carbon*, 2012, **50**, 1972-1980.
34 Z. M. Dang, J. K. Yuan, S. H. Yao, R. J. Liao. *Adv. Mater.,* 2013, **25**, 6334– 636
35 P. Xu, X. Han, C. Wang, D. Zhou, Z. Li, A. Wen, X. Wang, B. Zhang, *J. Phys. Chem. B*, 2008, **112**, 10443-10448.
36 H. Zhang, J. Zhang, H. Zhang. *Compos. Part A,* 2007, **38**, 602-608.
37 H. Zhang, J. Zhang, H. Zhang. *Comput. Mater. Sci.,* 2007, **38**, 857-864.
38 M. Hotta, M. Hayashi, M. T. Lanagan, D. K. Agrawal, K. Nagata, *ISIJ International*, 2011, **51**, 1766–1772.
39 J. G. Elton E. Kaxiras, *Nano Lett.* 2013, **13**, 898.
40 M.H. Al-Saleh, U. Sundararaj, *Carbon,* 2009, **47**, 1738-1746.
41 M.H Al-Saleh, W.H. Saadeh, U. Sundararaj, *Carbon,* 2013, **60**, 146-156.
42 N. Zhao, T. Zou, C. Shi, J. Li, W. Guo, *Mater. Sci. Eng. B,* 2006, **127**, 207-211.
43 B. Wen, X.X. Wang, W.Q. Cao, H.L. Shi, M.M. Lu, G. Wang, H.B. Jin, W.Z. Wang, J. Yuan, M.S. Cao, *Nanoscale*, 2014, 6, 5754-5761.
44 T.K. Gupta, B.P. Singh, R.B. Mathur, S.R. Dhakate, *Nanoscale*, 2014, 5, 842-851.
45 M.T. Chen, L. Zhang, S.S. Duan, S.L. Jing, H. Jiang, M.L. Luo, C.Z. Li, *Nanoscale*, 2014, 6, 3796-3803.


50x25mm (600 x 600 DPI)